Boosting the electrocatalytic glycerol oxidation performance with highly-dispersed Pt nanoclusters loaded on 3D graphene-like microporous carbon

Daewon Lee[a,1], Youngmin Kim[a,1], Yonghyun Kwon[b], Jongmin Lee[c], Tae-Wan Kim[d], Yuseong Noh[e], Won Bae Kim[e], Min Ho Seo[c,**], Kyoungsoo Kim[f,**], Hyung Ju Kim[a,g,*]

[a] Carbon Resources Institute, Korea Research Institute of Chemical Technology (KRICT), 141 Gajeong-ro, Yuseong-gu, Daejeon 34114, South Korea
[b] Center for Nanomaterials and Chemical Reactions, Institute for Basic Science (IBS), Daejeon 34141, South Korea
[c] Hydrogen & Fuel Cell Center, New & Renewable Energy Research Institute, Korea Institute of Energy Research (KIER), 20-41 Sinjaesaengeneogi-ro, Haseo-myeon, Buan-gu, Jellabuk-do 56332, South Korea
[d] Center for Convergent Chemical Process, Korea Research Institute of Chemical Technology (KRICT), 141 Gajeong-ro, Yuseong-gu, Daejeon 34114, South Korea
[e] Department of Chemical Engineering, Pohang University of Science and Technology (POSTECH), 77 Cheongam-Ro, Nam-gu, Pohang, Gyeongbuk 37673, South Korea
[f] Department of Chemistry, Chonbuk National University (CBNU), 567 Baekje-daero, Deokjin-gu, Jeonju-si, Jeollabuk-do 54896, South Korea
[g] Advanced Materials and Chemical Engineering, University of Science and Technology (UST), 113 Gwahangno, Yuseong, Daejeon 34113, South Korea

ARTICLE INFO

ABSTRACT

Preparing Pt nanostructure catalysts with better support materials is an efficient catalyst design strategy to develop high performance Pt-based electrocatalysts. Here we report for the first time a method to synthesize highly-dispersed Pt nanoclusters supported on microporous three-dimensional (3D) graphene-like carbon (3D-GLC) for use in the electrochemical oxidation reaction. The Pt nanoclusters loaded on 3D graphene-like carbon (Pt/3D-GLC) are synthesized by Ca^{2+}-exchanged beta zeolite template based carbon synthesis and subsequent Pt impregnation methods. Highly-dispersed Pt nanoclusters (*ca.* 1.25 ± 0.30 nm) loaded on the 3D-GLC having a large surface area (*ca.* 2910 m^2/g) demonstrate superior electrocatalytic performance for electrochemical glycerol oxidation reaction (GOR) over that of a commercial Pt/C catalyst. We hypothesize in this work that the improved GOR performance of Pt/3D-GLC is related to the increase of Pt active sites by decreasing Pt cluster size and the change in the physicochemical properties of the Pt by interaction between the Pt cluster and 3D-GLC. In addition, first-principle density functional theory (DFT) and *ab-initio* molecular dynamics (MD) simulations are performed to demonstrate that the finely-dispersed Pt nanoclusters on 3D-GLC support can give rise to excellent GOR activity in accordance with the enhanced adsorption behavior of glycerol on its Pt crystal surfaces.

1. Introduction

Recently, efforts have been devoted to developing efficient electrochemical conversion technologies to produce value-added chemicals and/or energy from biomass-derived oxygenates such as glycerol, hydroxymethylfurfural, furfural, glucose, and xylose [1–11]. In particular, glycerol is a valuable byproduct in the production of biodiesel and fatty acids [12–16]. Global glycerol production (4.3 million metric tonne (Mt) per year) exceeded the demand for glycerol (2.0 million Mt per year) in 2015 [17,18]. As the excess amount of glycerol increases, its price is expected to progressively fall, thereby becoming largely available for glycerol derivatives. The electrocatalytic oxidation process of glycerol is a promising technology that can produce valuable chemicals such as dihydroxyacetone, glyceraldehyde, glyceric acid, and glycolic acid by selective oxidation reaction and electrical energy by a full oxidization reaction [2,4,5,8,9]. Especially, electrocatalytic selective glycerol oxidation presents a promising method of co-producing renewable chemicals and hydrogen in an electrolysis cell system, which exploits oxidation chemistry and existing proton exchange membrane (PEM) technology to electrocatalytically convert glycerol into value-added chemicals and hydrogen [19]. In the electrochemical oxidation system, platinum (Pt) is commonly used to catalyze the oxidation reaction such as glycerol electrooxidation at the anodic side. Because of the high cost and rareness of Pt, there exist problems to massively use it

---

in practical applications. Therefore, many studies have been devoted to developing non-Pt-based electrocatalysts with low cost and earth-abundant materials to replace Pt [20]. In spite of recent efforts and advances for developing non-Pt-based electrocatalysts, Pt or Pt-based materials are still recognized as state-of-the-art electrocatalysts due to their kinetically excellent performance and catalytically stable characteristic for driving the electrochemical reactions such as alcohol oxidation. Therefore, it is desirable to design and develop more effective Pt-based electrocatalysts that can be produced in a cost-effective and facile manner for electrochemical reactions.

In order to design high performance Pt-based electrocatalysts, several approaches such as synthesizing nanomaterials with various shapes and structures [21,22], alloying with other metals [7,23–25], and employing better support materials [26–33] have been mainly attempted to enhance the activity and stability of Pt. In particular, amorphous carbon such as Vulcan XC-72 carbon black is generally used as the support material of Pt for catalyzing the electrochemical oxidation reaction. However, this commercial amorphous carbon material has a relatively low surface area of less than $300 \, m^2/g$ [27–29]. This low surface area may be insufficient to prepare a catalyst having large electrochemical active surface (EAS) area with a highly-dispersed Pt nanostructure. As a potential candidate, two-dimensional (2D) graphene has been studied as a Pt catalyst support due to its excellent physicochemical features such as a large surface area (theoretically, *ca.* $2630 \, m^2/g$), high thermal and electrical conductivity, and remarkable mechanical strength [29,34]. This 2D graphene support has several advantages to design and develop highly efficient supported Pt electrocatalysts for electrochemical reactions: (1) highly dispersed small Pt nanoparticles (2–3 nm) loaded on a graphene support with large surface area, which is related to the EAS area [28]; (2) bonding strength between the Pt metal and graphene support, which is associated with the probability of Pt agglomeration and the Pt particle size control [35,36]; and (3) a change in the electronic structure of the Pt onto the graphene support, which affects the adsorbate binding energy [36]. However, it has been reported that the surface area of the graphene support decreases considerably due to the restacking effect of individual graphene sheet by van der Waals force and π-π interaction [37]. This restacking of the 2D graphene sheet has been an obstacle for its use as an effective electrochemical carbon support because it would decrease the EAS area of Pt, making one side of Pt supported on graphene unavailable [38]. Therefore, more efficient catalyst design strategies in terms of how to minimize the restacking effect of graphene and maximize the advantages of using graphene itself as the support are required for developing high performance graphene support-based electrocatalysts.

Here we report a novel and efficient strategy to prepare highly-dispersed Pt nanoclusters supported on microporous three-dimensional (3D) graphene-like carbon (3D-GLC) for the first time. The Pt nanoclusters loaded on 3D graphene-like carbon (Pt/3D-GLC) are prepared by zeolite template based carbon synthesis and subsequent Pt impregnation methods (see Fig. 1). This synthetic approach can be useful to overcome the restacking problem of the 2D graphene support. The highly-dispersed Pt nanoclusters (*ca.* 1.25 ± 0.30 nm) on 3D graphene-like carbon demonstrate about 1.6 times higher electrocatalytic activity for electrochemical glycerol oxidation reaction (GOR) than that of a commercial Pt/C catalyst (BASF). In this work, we demonstrate how highly-dispersed Pt nanoclusters are formed on 3D-GLC and why the Pt nanoclusters loaded on 3D-GLC exhibit superior electrocatalytic performance compared to the conventional amorphous carbon-supported Pt catalyst for the GOR. In addition, we perform first-principle density functional theory (DFT) and *ab-initio* molecular dynamics (MD) simulations to understand fundamentals about electrocatalytic GOR performance enhancement by decreasing Pt cluster size and the formation of an interface between the Pt nanocluster and 3D-GLC. In this study, theoretical insights obtained for our designed catalytic material are also related to improvement of experimentally-obtained catalytic performance for the electrochemical GOR.

2. Experimental

2.1. Synthesis of 3D-GLC and Pt/3D-GLC

Microporous 3D-GLC was synthesized through a hard-templating strategy where beta zeolite and ethylene were used as a sacrificial template and a carbon source, respectively [39,40]. The beta zeolite (Si/Al = 14, H^+ form) was purchased from Tosoh. Prior to the carbon synthesis, the zeolite was ion-exchanged with Ca^{2+} two times using a 0.5 M aqueous solution of $CaCl_2 \cdot 6H_2O$ (Sigma-Aldrich), and then calcined at 550 °C under an air atmosphere. For carbon deposition into micropores of Ca^{2+}-beta zeolite, 10 g of the zeolite was placed in a quartz plug-flow reactor equipped with a 15 mm diameter fritted disk. The reactor was then heated to 650 °C with a heating rate of 5 °C/min while a dry N_2 flow was passed through the zeolite bed. After stabilizing the temperature at 650 °C, the N_2 flow was combined with ethylene gas and H_2O vapor. The total gas flow rate was $800 \, cm^3/min$, and the volumetric ratio of N_2, ethylene, and H_2O was 10/87/3, which was controlled by a mass flow controller (M2030V, Line Tech). The gas flow was continued for 4 h to achieve full carbon deposition. Feeding of the ethylene and H_2O vapor was then stopped, and the reactor temperature was further increased to 900 °C under a dry N_2 flow. The temperature was maintained for 2 h to rigidify the carbon frameworks formed in the zeolite. After cooling the reactor, the resultant sample was repeatedly treated in a 0.3 M HF/0.15 M HCl solution for removal of the zeolite template. The final 3D-GLC products were collected using filtration, washed with deionized water, and dried at 100 °C. The carbon yield was approximately 0.32 g per 1 g zeolite.

The loading of Pt nanoclusters on the 3D-GLC was carried out by incipient wetness impregnation using an acetone solution of $H_2PtCl_6 \cdot 6H_2O$ (Sigma-Aldrich), following the procedure in the literature [26]. In a typical experiment, 0.148 g of $H_2PtCl_6 \cdot 6H_2O$ was impregnated in 0.5 g of carbon in order to provide 10 wt% Pt content. After being dried in a convection oven at 100 °C for 12 h, the Pt-impregnated carbon sample was placed in a U-tube flow reactor equipped with a fritted disk. The reactor was then heated to 300 °C at a ramping rate of 2 °C/min under a H_2 flow (60 cm^3/min). The sample was subsequently degassed at 300 °C for 2 h to remove chemisorbed hydrogen.

2.2. Catalyst characterization

A double Cs-corrected transmission electron microscopy (TEM) (Titan G2 60-300S, FEI) with an acceleration voltage of 300 kV was used to collect TEM images and high-angle annular dark-field scanning transmission electron microscopy (HAADF-STEM) images with corresponding energy dispersive X-ray spectroscopy (EDS) mapping results. A scanning electron microscopy (SEM) (Verios 460, FEI) with a landing voltage of 1 kV in deceleration mode was used to take SEM images. The ^{13}C solid-state magic-angle spinning (MAS) nuclear magnetic resonance (NMR) spectrum was recorded at 9.4 T using a NMR spectrometer (AVANCE III HD, Bruker). An Ar adsorption-desorption isotherm curve was obtained at a liquid Ar temperature (−186 °C) from a surface area and porosimetry measurement system (ASAP 2020, Micromeritics). The surface area was determined using the Brunauer-Emmett-Teller (BET) method, and the pore size distribution and pore volume were derived using nonlocal density functional theory. X-ray diffraction (XRD) spectra were acquired at a tube voltage of 40 kV and a tube current of 40 mA by using a multipurpose X-ray diffraction system (Ultima IV, Rigaku) with a Cu Kα source. A high-resolution Raman/photo-luminescence system (LabRAM HR Evolution, Horiba) with a laser excitation wavelength of 514 nm was used to record Raman spectra. A multipurpose X-ray photoelectron spectrometer (Sigma Probe, Thermo Fisher Scientific) with an Al Kα source was exploited in order to obtain the X-ray photoelectron spectroscopy (XPS) spectra. The 7D beamline of Pohang Accelerator Laboratory equipped with a Si (111) double crystal monochromator (PLS-II, 3.0 GeV, Republic of Korea) was utilized in
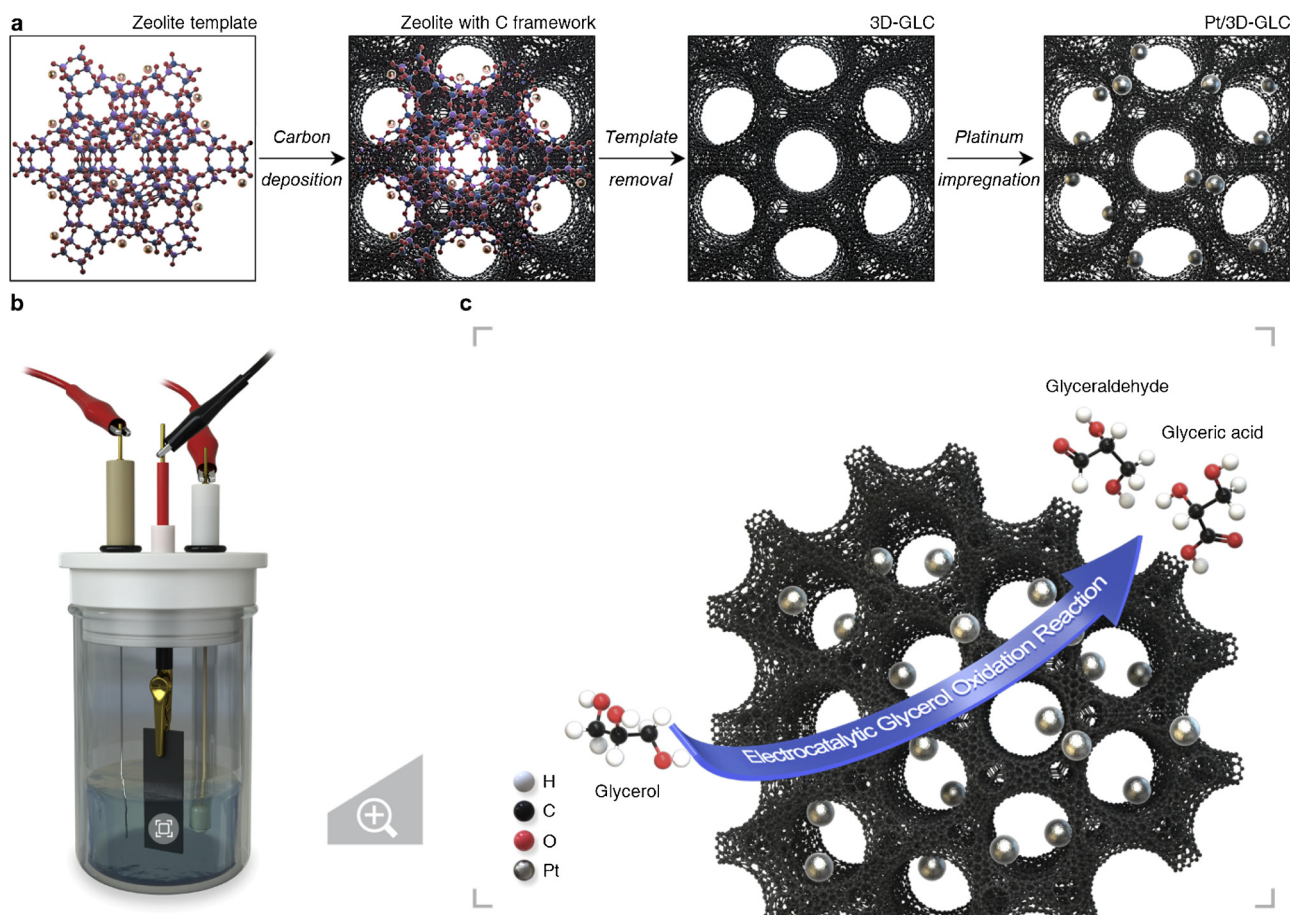
Fig. 1. Schematic illustrations for the synthesis of Pt/3D-GLC and its electrochemical application. a–c, Schematic illustrations showing the fabrication of 3D microporous graphene-like carbon (3D-GLC) and Pt impregnation on 3D-GLC (Pt/3D-GLC) (a), an electrochemical batch reactor system (b), and electrocatalytic glycerol oxidation reaction (GOR) over Pt/3D-GLC (c).

performing a synchrotron-based X-ray absorption spectroscopy (XAS) analysis at the L_3-edge of Pt (11,564 eV), comprising X-ray absorption near the edge structure (XANES) and extended X-ray absorption fine structure (EXAFS). Fourier-transform infrared (FT-IR) spectra were recorded using a Fourier-transform infrared spectrometer (ALPHA, Bruker). A high-resolution thermogravimetric analyzer (TG209 F1 Libra, NETZSCH) was exploited to acquire thermogravimetric analysis (TGA) profiles with a ramping rate of 5 °C/min under air flow. The EDS analysis was performed on an energy dispersive X-ray spectrometer (Quantax 200, Bruker) equipped with a Si drift detector. Hydrogen (H$_2$) chemisorption was carried out at room temperature using a lab-made glass rig for volumetric adsorption. Before the measurement, Pt-loaded samples were reduced at 300 °C under H$_2$ flow (99.999%) that passed through an MnO/SiO$_2$ trap for removal of trace oxygen. To exclude the effect of the physisorbed hydrogen gas on the carbon supports, the sample was outgassed at room temperature after the first adsorption measurement, and then hydrogen adsorption on the sample was conducted repeatedly. The resultant adsorption isotherms were obtained based on the difference of the adsorption amount between the two measurements (*i.e.*, the first adsorption and subseqent back-sorption). The hydrogen chemisorption in H/Pt was determined by extrapolation of the adsorption isotherm to zero pressure. This value refers to the total amount of chemisorbed H$_2$.

2.3. Electrochemical performance measurement in an electrochemical half-cell system

Electrocatalytic performance for GOR was measured in a three-electrode cell system at room temperature using a potentiostat (ZIVE

MP2A, WonATech). Pt wire and Ag/AgCl/1 M KCl served as counter and reference electrodes, respectively. A catalyst-coated glassy carbon electrode was used as a working electrode. For the fabrication of the working electrode, catalyst inks were first prepared; synthesized 10 wt % Pt/3D-GLC, 3D-GLC, commercial 10 wt% Pt/C (BASF), and Vulcan XC-72 (Premetek) were dispersed in mixed solutions of distilled water, ethanol (95.0%, Samchun Pure Chemical), and 5 wt% Nafion® ionomer solution (D521, DuPont) *via* sonication for 1 h. For the electrocatalytic GOR, the produced catalyst ink was relocated onto a glassy carbon disk working electrode surface (with a geometric area of *ca.* 0.071 cm^2), and a thin catalyst layer (with a loaded amount of *ca.* 0.218 mg/cm^2) was deposited on the surface of the working electrode after a drying process. Cyclic voltammetry (CV) was implemented in N$_2$-purged 2 M glycerol (≥ 99.0%, Junsei Chemical) + 0.5 M H$_2$SO$_4$ solution (Samchun Pure Chemical) or 0.5 M H$_2$SO$_4$ solution only over a potential range of 0.036–1.236 V (*vs.* SHE) at a scan rate of 50 mV/s.

2.4. Electrochemical performance measurement in an electrochemical batch reactor system

The three-electrode cell system, which comprises catalyst-coated carbon paper as a working electrode, a Pt wire counter electrode, and an Ag/AgCl/1 M KCl reference electrode, was connected to the potentiostat to measure electrocatalytic performance in an electrochemical batch reactor system. The catalyst-coated carbon paper as the working electrode was made by spray coating a catalyst ink solution onto carbon paper (TGP-H-090, Toray). This catalyst ink was prepared by dispersing 10 wt% Pt/3D-GLC or 10 wt% Pt/C in a mixture of distilled water, 2-propanol (99.5%, Samchun Pure Chemical), and 5 wt%

Nafion® ionomer solution *via* sonication for 1 h. After spray coating the prepared ink solution, a thin catalyst layer was formed on the carbon paper electrode (with a geometric area of *ca.* 2 cm^2), and the catalyst-coated carbon paper was dried in a convection oven at 100 °C for 1 h. Eventually, a thin catalyst layer with a catalyst loaded amount of *ca.* 2.25 mg/cm^2 was fabricated on the conducting carbon paper electrode. Electrocatalytic performance for the GOR was evaluated in a 7 mL solution of 0.1 M glycerol/0.5 M H$_2$SO$_4$ at a constant reaction temperature of 60 °C. Chronoamperometry was performed at a constant potential of 1.136 V (*vs.* SHE) for 6 h. After the electrocatalytic GOR, the liquid reaction products were collected and analyzed by injecting 10 μL of a liquid sample into a high-performance liquid chromatography (HPLC) equipped with a binary HPLC pump (1525, Waters), a refractive index detector (2414, Waters), an ultraviolet/visible detector with a wavelength of 210 nm (2487, Waters), and an ion-exchange ligand exchange column (Hi-Plex H, Agilent Technologies) with 0.005 M H$_2$SO$_4$ aqueous solution (Samchun Pure Chemical) as an eluent at a flow rate of 0.3 mL/min and a column oven temperature of 60 °C. An external calibration method was exploited in order to determine the glycerol conversion and the selectivities of the reaction products.

2.5. Computational modeling and design

The Vienna *Ab-initio* Simulation Package (VASP) program was conducted for first-principle density functional theory (DFT) calculations [41]. The electron exchange-correlation energy used Perdew, Burke, and Ernzerhof (PBE) functions [42] with Projector Augmented Wave (PAW) pseudopotentials [43]. Before designing the carbon-supported Pt nanoparticle slab models, Pt$_{55}$ and Pt$_{13}$ clusters and a glycerol molecule were designed and fully relaxed in a vacuum unit cell of a cubic box having 50 Å, 50 Å, and 10 Å lengths, respectively. Pt$_{13}$ and Pt$_{55}$ denote the number (13 and 55) of Pt atoms in a cuboctahedral particle structure, respectively. The gamma point mesh was used in (1 × 1 × 1) **k**-points, and the cutoff energy used was 520 eV. Moreover, (9 × 8) pristine graphite and graphene surfaces were designed as a support after fully optimizing bulk graphite with a gamma point mesh of (25 × 25 × 25). The graphite and graphene slab models were designed with a z-axis length of 50 Å. The bottom two layers of graphite consisting of three layers of graphene were fixed to simulate the bulk surface whereas the graphene of one layer was fully relaxed. Next, cuboctahedral Pt$_{13}$ and Pt$_{55}$ clusters [44] were put on the surfaces of graphene and graphite supports in a vacuum slab to avoid interaction between the top and bottom layers, and then the designed models were simulated with a periodic boundary condition with the gamma point (1 × 1 × 1). In order to comprehend the GOR activities of Pt clusters supported on graphite or graphene, the most favorable sites for glycerol adsorption were investigated on the cuboctahedron Pt clusters having (100) and (111) crystal surfaces. Binding energies (ΔE_{BE}) of the glycerol molecule onto the Pt surface were calculated after designing the glycerol molecules put onto Pt(100) and Pt(111) crystal surfaces. We also carried out *ab-initio* molecular dynamics (MD) simulations [45] in order to find the thermodynamically most favorable adsorbent sites on the Pt crystal surfaces. *Ab-initio* MD simulations were conducted for a time period of 250 fs, and we used the canonical ensemble [45] to prevent molecules from breaking at a fast moving velocity. The adsorption energy of glycerol onto the carbon-supported Pt surface (ΔE_{ads}) was defined and estimated according to Eq. (1),

$$\Delta E_{ads} = \Delta E_{0\_PtC/Glycerol} - \Delta E_{0\_Glycerol} - \Delta E_{0\_PtC} \tag{1}$$

where Δ$E_{0\_PtC/Glycerol}$, Δ$E_{0\_Glycerol}$, and ΔE_{0_PtC} are the total energies obtained from the DFT calculation for the glycerol-deposited Pt cluster on graphite and graphene, the single glycerol molecule, and Pt cluster on graphite or graphene, respectively. Eventually, we determined all of the ΔE_{ads} values for the graphene and graphite supported Pt$_{13}$ or Pt$_{55}$ clusters in order to elaborate the enhanced GOR performance of Pt/3D-

GLC compared to conventional Pt/C.

3. Results and discussion

3.1. Structural and chemical analyses of synthesized 3D-GLC

We prepared a 3D-GLC material through carbonization of ethylene within Ca^{2+}-exchanged beta zeolite and the subsequent removal of the zeolite (see Experimental section in the Supporting information for details). The final product is composed of aggregates of carbon crystals with diameters of 50–200 nm (Fig. S1). The overall morphology of 3D-GLC is quite similar to that of the beta zeolite used in the carbon synthesis. In the TEM image of the carbon (Fig. S2), lattice fringes with 1.11 nm spacing (*d*) can be observed. The results of the electron microscopic investigation indicate that the ordered porous structure of the zeolite template is faithfully replicated by the carbon frameworks. The bonding nature in the carbon frameworks was revealed by ^{13}C solid-state MAS NMR spectroscopy (Fig. S3). The spectrum shows predominant *sp*^{2}-carbon peaks at chemical shifts of 123 and 129 ppm, which can be assigned to a 6-membered carbon ring and a defective distorted carbon ring, respectively [46]. It is worth noting that the periodic porous structure of the 3D-GLC is mainly built of *sp*^{2}-carbon rings. The curvature of the pore surfaces might bring about the formation of defective rings, such as 5- or 7-membered ring. The further structural characterization was performed using argon (Ar) sorption isotherm (Fig. S4a). The carbon exhibits type I isotherm, which is characteristic of a microporous material. The pore size distribution (Fig. S4b) derived from the isotherm shows a very narrow peak centered at 0.89 nm, with a small shoulder in a range of 1.1–2.6 nm. The BET surface area and the total pore volume are 2910 m^2/g and 1.3 cm^3/g, respectively.

3.2. Morphological and chemical analyses of Pt-impregnated 3D-GLC

In order to evaluate the electrocatalytic performance in GOR, the 3D-GLC sample was impregnated with 10 wt% Pt. The Pt supporting process involved incipient-wetness impregnation of acetone solution containing H$_2$PtCl$_6$, and subsequent reduction. The loaded amount of Pt in the resultant Pt/3D-GLC was determined using a TGA and EDS. Through the complete combustion of respective carbon supports, TGA curves for Pt/3D-GLC and Pt/C (commercial, 10 wt%) revealed that the catalysts contain a similar amount of Pt (Fig. S5). In addition, the Pt content in Pt/3D-GLC estimated from TGA and EDS was 11.3 and 10.1 wt%, respectively (Table S1).

The morphology of the Pt/3D-GLC was examined through an electron microscopy analysis along with a commercial Pt/C. The HAADF-STEM images of Pt/3D-GLC distinctly exhibit the presence of finely dispersed Pt nanoclusters on 3D-GLC (Figs. 2a and S6) in contrast to sparsely aggregated Pt nanoparticles of commercial Pt/C (Figs. 2b and S8). In order to compare the uniformity of the Pt particle size, we calculated and presented histograms showing Pt particle size distributions and mean Pt particle sizes in Fig. 2a and b, using 160 different Pt particles displayed in respective HAADF-STEM images for Pt/3D-GLC and Pt/C. Note that the length-number mean diameter (d_{LN}) was calculated according to Eq. (2),

$$d_{LN} = \frac{\sum n_i d_i}{\sum n_i} \tag{2}$$

where n_i is the number of particles of a diameter d_i [47]. The estimated d_{LN} values for Pt/3D-GLC and Pt/C were 1.25 ± 0.30 and 3.46 ± 1.67 nm, respectively, which indicate that the synthesized Pt/3D-GLC possesses small Pt nanoclusters with a narrow particle size distribution compared to commercial Pt/C. As shown in Fig. S10, the Pt particle size values determined by H$_2$ chemisorption experiments were 1.68 and 3.64 nm for Pt/3D-GLC and Pt/C, respectively, which were
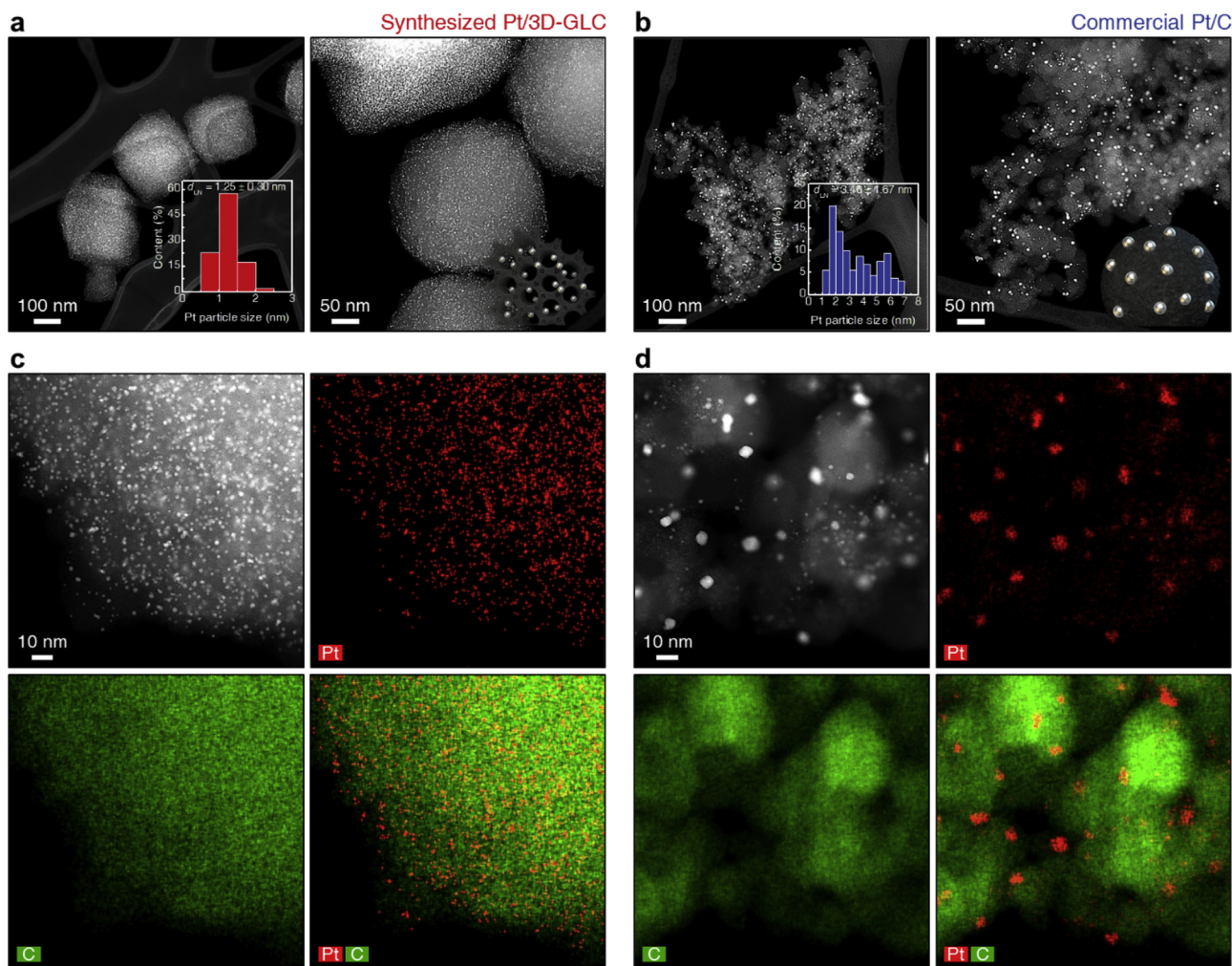
Fig. 2. Morphological analysis of synthesized Pt/3D-GLC and commercial Pt/C using electron microscopy. a,b, HAADF-STEM images of Pt/3D-GLC (a) and Pt/C (b). Inset: Pt particle size distribution (left) and schematic illustration (right) of Pt/3D-GLC and Pt/C. c,d, EDS elemental mapping of Pt, C, and a composite of Pt and C for Pt/3D-GLC (c) and Pt/C (d).

similar to those obtained in the HAADF-STEM analysis. The interaction between Pt and 3D-GLC during catalyst preparation may contribute to the formation of highly dispersed Pt nanoclusters on 3D-GLC. EDS elemental mapping results for Pt and/or C, coupled with corresponding HAADF-STEM images, demonstrate a notable distinction in distribution and size of Pt particles between prepared Pt/3D-GLC and commercial Pt/C (Figs. 2c, d, S7, and S9).

3.3. Physicochemical analyses of Pt/3D-GLC via various spectroscopic methods

As shown in Fig. 3, detailed analyses using various spectroscopic methods were conducted to investigate the physicochemical properties of the synthesized Pt/3D-GLC. In line with the lattice fringes observed in the TEM analysis (Fig. S2), 3D-GLC shows a characteristic XRD peak at around 7.9° (Fig. 3a), which reveals a highly ordered microporous structure of 3D-GLC [39]. Additionally, the absence of a (002) diffraction peak at around 26° in the XRD pattern for 3D-GLC, which represents stacked graphene layers, suggests that 3D-GLC is composed of single layer graphene [48]. After the impregnation process of Pt nanoclusters on the 3D-GLC, these XRD characteristic peaks exhibiting the unique carbon structure are maintained in the XRD pattern for Pt/3D-GLC. The Pt/3D-GLC also displays characteristic XRD peaks of Pt in accordance with the reference crystallographic data for face-centered cubic (*fcc*) Pt (JCPDS No. 04-0802). As shown in Fig. 3a, the

commercial Pt/C (Vulcan XC-72 carbon-supported Pt) also showed a typical XRD pattern representing the characteristics of both Vulcan XC-72 carbon support and *fcc* Pt.

Raman spectroscopy in Fig. 3b provides further insight into structural and chemical properties of the synthesized graphene-like materials (*i.e.* 3D-GLC and Pt/3D-GLC). In contrast to the Raman spectra obtained from Vulcan XC-72 and Pt/C, both 3D-GLC and Pt/3D-GLC showed distinctive Raman spectra with prominent *D* and *G* bands. The *D* band is originated from the defect-induced features of graphitic materials (*e.g.* odd-numbered carbon rings), and the *G* band is associated with the existence of sp^2-carbon networks or graphene sheets [48]. The broad *D* bands in the measured Raman spectra for 3D-GLC and Pt/3D-GLC indicate that it contains 5- or 7-membered carbon rings [49]. Compared to the Vulcan XC-72 and Pt/C, the existence of nano-sized graphene (nano-graphene) layers in 3D-GLC and Pt/3D-GLC results in an upshift of the *G* bands at $1577\,cm^{-1}$ [48]. Additional spectroscopic investigation using FT-IR spectroscopy (Fig. S11) reveals the existence of synthesized graphene in 3D-GLC and Pt/3D-GLC by confirming the absorption peak for the skeletal vibration of graphene sheets at $1600\,cm^{-1}$ [50]. These characterization results suggest that the synthesized 3D-GLC and Pt/3D-GLC have unique carbon structures that consist of curved nano-graphene single layers without any stacked graphene layers [39,40]. It is worthwhile to note that the Raman spectra can also provide information about the interaction between 3D-GLC and impregnated Pt nanoclusters. The ratio of intensities of the *D*
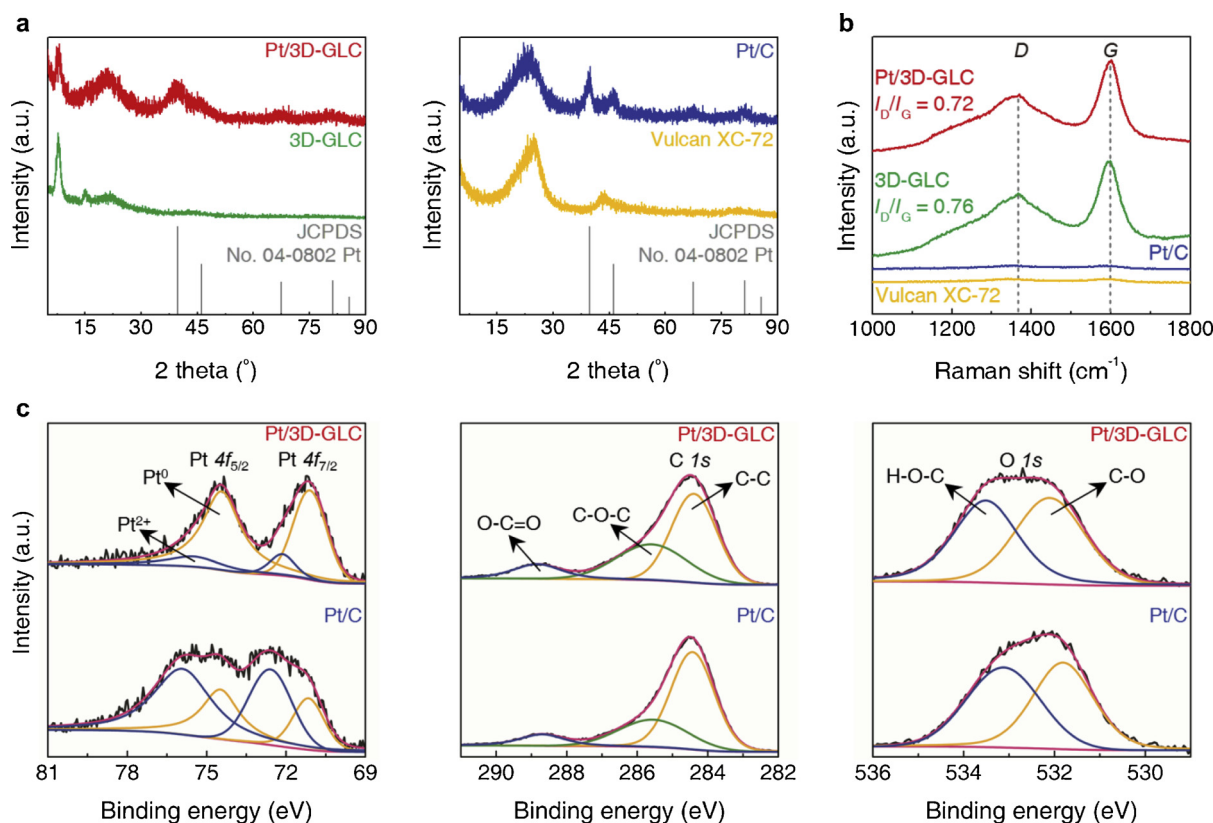
Fig. 3. Structural, chemical, and electronic analyses of Pt/3D-GLC and Pt/C. a, XRD spectra of Pt/3D-GLC, 3D-GLC, Pt/C, and Vulcan XC-72. As a reference, the crystallographic data for Pt (JCPDS No. 04-0802) are displayed. b, Raman spectra from Pt/3D-GLC, 3D-GLC, Pt/C, and Vulcan XC-72. Note that the position of the *D* and *G* bands and the ratios of the intensities of the *D* and *G* bands are represented. c, High-resolution XPS spectra in the regions of Pt *4f*, C *1s*, and O *1s* peaks for Pt/3D-GLC and Pt/C.

and *G* bands (I_D/I_G) is used as an indicator of the structural disorder in graphitic materials: a higher I_D/I_G value generally means an increase of structural disorder [51]. The estimated I_D/I_G values for 3D-GLC and Pt/3D-GLC are 0.76 and 0.72, respectively. The decreased I_D/I_G value for Pt/3D-GLC implies that impregnated Pt nanoclusters are dispersed on the defect sites of 3D-GLC and therefore suppress the characteristic vibrations under Pt nanoclusters [52]. Furthermore, it has been reported that charge transfer between graphitic materials and supported metal nanoparticles leads to shifts of *D* and *G* bands [53]. Compared to the *D* (1367 cm^{-1}) and *G* (1599 cm^{-1}) bands for 3D-GLC, the Raman spectrum for Pt/3D-GLC reveals shifted *D* and *G* bands at 1370 and 1600 cm^{-1}, respectively. This upshift of both the *D* and *G* bands suggests electron transfer from graphitic 3D-GLC to Pt nanoclusters [53].

XPS was performed to identify the surface chemical states and electronic structures of the prepared Pt/3D-GLC and commercial Pt/C samples. Note that all the XPS binding energies were referenced by using the C *1s* line (284.5 eV). We present the high-resolution XPS spectra in the Pt *4f*, C *1s*, and O *1s* regions for Pt/3D-GLC and Pt/C (Fig. 3c) and tabulate the respective peak assignment, binding energy, and relative area of deconvoluted peaks from the XPS spectra for Pt/3D-GLC and Pt/C (Table 1). As presented in the high-resolution Pt *4f* spectra of Fig. 3c for Pt/3D-GLC and Pt/C, spin-orbit splitting doublet Pt *4f*$_{7/2}$ and Pt *4f*$_{5/2}$ peaks were deconvoluted into zero-valent Pt and Pt^{2+} (PtO or Pt(OH)$_2$), respectively [23]. For the Pt *4f* spectra, there exists a difference in the Pt oxidation state between Pt/3D-GLC and Pt/C; the metallic Pt (Pt^0) is dominant ($\approx$ 83.45%) in the Pt/3D-GLC, but the oxidized Pt phase (Pt^{2+}) is predominant ($\approx$ 64.69%) in the Pt/C (Table 1) [54,55]. Compared to Pt^0 (71.150 and 74.480 eV) and Pt^{2+} (72.590 and 75.920 eV) peaks for Pt/C, the Pt^0 (71.102 and 74.432 eV) and Pt^{2+} (72.137 and 75.467 eV) peaks for Pt/3D-GLC were shifted to lower binding energies. This can be ascribed to the electron transfer

from 3D-GLC to Pt nanoclusters in correspondence with the results from the Raman spectra (*i.e.* upshift of *D* and *G* bands). The Pt valence band is possibly filled with electrons donated by 3D-GLC, which can give rise to a decrease of electron binding energies in the Pt core level [8,52]. For the C *1s* region, the recorded spectra were divided into three peaks for sp^2-hybridized C−C (284.391–284.430 eV) and two oxygen-containing functional groups of C−O−C (285.543–285.591 eV) and O−C=O (288.693–288.832 eV). It is worthwhile to note that the relative amount of oxygenated functional groups in Pt/3D-GLC ($\approx$ 45.68%) is higher than that in Pt/C ($\approx$ 36.61%). We believe that these abundant oxygen functional groups affect the interaction between the Pt nanoclusters and the 3D-GLC support during the Pt impregnation, eventually creating fine Pt nanoclusters uniformly dispersed on 3D-GLC [27]. The high-resolution O *1s* spectra consisting of two deconvoluted peaks assigned to C−O (531.810–532.104 eV) and H−O−C (533.117–533.510 eV) bonds did not show substantial differences between Pt/3D-GLC and Pt/C.

3.4. Synchrotron-based analysis on the local atomic structure of Pt/3D-GLC

Synchrotron-based XAS, including two complementary techniques of XANES and corresponding EXAFS, was performed to investigate and understand the local atomic structure of Pt/3D-GLC in comparison with that of Pt/C (Figs. 4, S12–S16, and Table 2 and 3). The normalized Pt L_3-edge XANES spectra obtained from Pt/3D-GLC, Pt/C, and reference materials (Pt foil and PtO$_2$) present differences between Pt/3D-GLC and Pt/C with respect to white-line (WL) intensity and threshold energy (E_0). The WL intensity indicating the intensity of humps at the Pt L_3-edge is closely related with the electronic transition from $2p_{3/2}$ to $5d$ at the Pt L_3-edge. This is correlated with the electron occupancy in the Pt $5d$ states: the decreased WL intensity reflects higher electron filling of

Table 1
Summary of peak assignments, binding energy, and relative area of the deconvoluted peaks from high-resolution XPS spectra of Pt/3D-GLC and Pt/C.

Samples	Pt *4f*				C *1s*			O *1s*		
	Peaks		Binding energy (eV)	Relative area (%)	Peaks	Binding energy (eV)	Relative area (%)	Peaks	Binding energy (eV)	Relative area (%)
Pt/3D-GLC	Pt *4f_{7/2}*	Pt^0	71.102	33.58 (82.59)[a]	C−C	284.391	54.32	C-O	532.104	50.49
		Pt^{2+}	72.137	7.08 (17.41)[a]	C−O−C	285.591	34.02	H-O-C	533.510	49.51
	Pt *4f_{5/2}*	Pt^0	74.432	50.02 (84.30)	O−C═O	288.832	11.66			
		Pt^{2+}	75.467	9.32 (15.70)						
Pt/C	Pt *4f_{7/2}*	Pt^0	71.150	13.68 (35.40)	C−C	284.430	63.39	C-O	531.810	50.04
		Pt^{2+}	72.590	24.96 (64.60)	C−O−C	285.543	27.23	H-O-C	533.117	49.96
	Pt *4f_{5/2}*	Pt^0	74.480	21.61 (35.22)	O−C═O	288.693	9.38			
		Pt^{2+}	75.920	39.75 (64.78)						

[a] Relative % of the Pt^0 and Pt^{2+} species for each of Pt *4f_{7/2}* and Pt *4f_{5/2}*.

Pt *5d* orbitals [56]. Compared to the WL intensity value of 1.64 for the Pt/C, the decreased WL intensity value of 1.58 for the Pt/3D-GLC can be attributed to the 5*d* electron filling of the Pt by electron donation from 3D-GLC (Fig. 4a). This phenomenon can be explained on the basis of the previous Raman and XPS analysis results. The threshold energy, E_0 value, which was determined at the maximum derivative of the edge, provides additional information about the oxidation state of Pt. The E_0 of Pt/3D-GLC (11,564.3 eV) is closer to that of Pt foil (11,564.0 eV), while Pt/C exhibits an E_0 of 11,565.2 eV, which lies between Pt/3D-GLC and PtO$_2$ (11,566.6 eV) [57]. This indicates that metallic Pt species are relatively dominant in Pt/3D-GLC compared to the Pt/C [58].

The k^3-weighted raw EXAFS function and corresponding Fourier-transform of the EXAFS (FT-EXAFS) spectra at the Pt L_3-edge are presented in Figs. S16 and 4 b, respectively. In Fig. 4b, a Pt−Pt scattering peak in Pt metal foil appeared in the range of 2–3 Å, and a peak of Pt−O contribution in PtO$_2$ reference is seen in the range of 1–2 Å. For supported Pt catalysts, they contain both Pt−Pt and Pt−O contributions. The values of average coordination numbers and bond distances from EXAFS curve fitting are given in Table 3. The real and imaginary parts with the fitted curves for the samples are presented in Fig. S16. The fitting results showed that two different Pt−O contributions were present in the Pt/C and Pt/3D-GLC catalysts. The first Pt−O bond with ~2.0 Å, which is similar to the distance found in PtO$_2$, originates from partially oxidized Pt surfaces. The second Pt−O bond with a bond length of ~2.6 Å is attributed to the coordination of the Pt atom with oxygen of the support *via* metal-support interaction [59]. The amount of Pt−O contributions appears to be higher for the Pt/C compared to the Pt/3D-GLC, which is consistent with the XANES results. The EXAFS fitting results showed that both the Pt−Pt coordination number and the Pt−Pt bond distance in 3D-GLC supported Pt catalyst (3.3 and 2.71 Å) are decreased compared to those in the conventional Vulcan XC-72 carbon supported Pt catalyst (5.0 and 2.74 Å), suggesting much smaller size of Pt clusters on the 3D-GLC support. This also agrees well with our STEM observation.

Table 2
Summary of WL intensity and E_0 from normalized Pt L_3-edge XANES spectra of Pt/3D-GLC, Pt/C, PtO$_2$, and Pt foil.

Samples	WL intensity (a.u.)	E_0 (eV)
Pt foil	1.27	11,564.0
Pt/3D-GLC	1.58	11,564.3
Pt/C	1.64	11,565.2
PtO$_2$	2.54	11,566.6

Table 3
Summary of EXAFS fitting results for Pt/3D-GLC and Pt/C with reference materials of PtO$_2$ and Pt foil.

Samples	Shell	N[a]	R[b] (Å)	R-factor[c] (%)
Pt foil	Pt−Pt	12[d]	2.765 ± 0.001	0.09
PtO$_2$	Pt−O$_{1st}$	2[d]	1.725 ± 0.038	1.35
	Pt−O$_{2nd}$	4[d]	2.015 ± 0.009	
	Pt−Pt$_{1st}$	2[d]	3.098 ± 0.008	
	Pt−Pt$_{2nd}$	8[d]	3.813 ± 0.040	
Pt/C	Pt−O$_{1st}$	1.44 ± 0.05	2.010 ± 0.002	0.3
	Pt−O$_{2nd}$	0.26 ± 0.04	2.609 ± 0.007	
	Pt−Pt	5.03 ± 0.26	2.742 ± 0.003	
Pt/3D-GLC	Pt−O$_{1st}$	1.22 ± 0.04	2.032 ± 0.002	0.3
	Pt−O$_{2nd}$	0.13 ± 0.01	2.651 ± 0.005	
	Pt−Pt	3.29 ± 0.17	2.712 ± 0.003	

[a] Coordination number.
[b] Bond distance.
[c] R-factor is a goodness of curve fitting.
[d] Fixed value.

3.5. Electrocatalytic performance measurement of Pt/3D-GLC toward GOR in both electrochemical half-cell and batch reactor systems

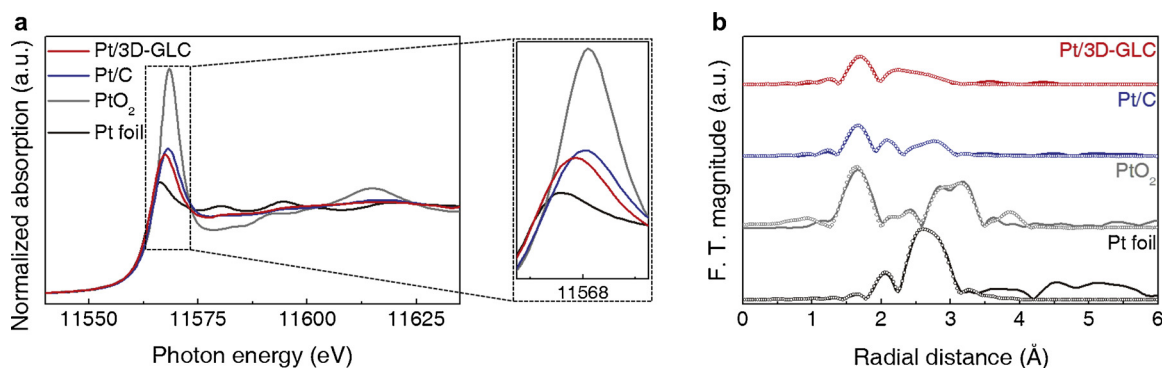The electrochemical performance of the synthesized Pt/3D-GLC

Fig. 4. Synchrotron-based XAS analysis on Pt/3D-GLC and Pt/C. a,b, Normalized Pt L_3-edge XANES (a) and the magnitude of k^3-weighted FT-EXAFS spectra (b) of Pt/3D-GLC, Pt/C, PtO$_2$, and Pt foil. Note that experimental and fitting results for FT-EXAFS are discriminately displayed as solid lines and circle markers, respectively.
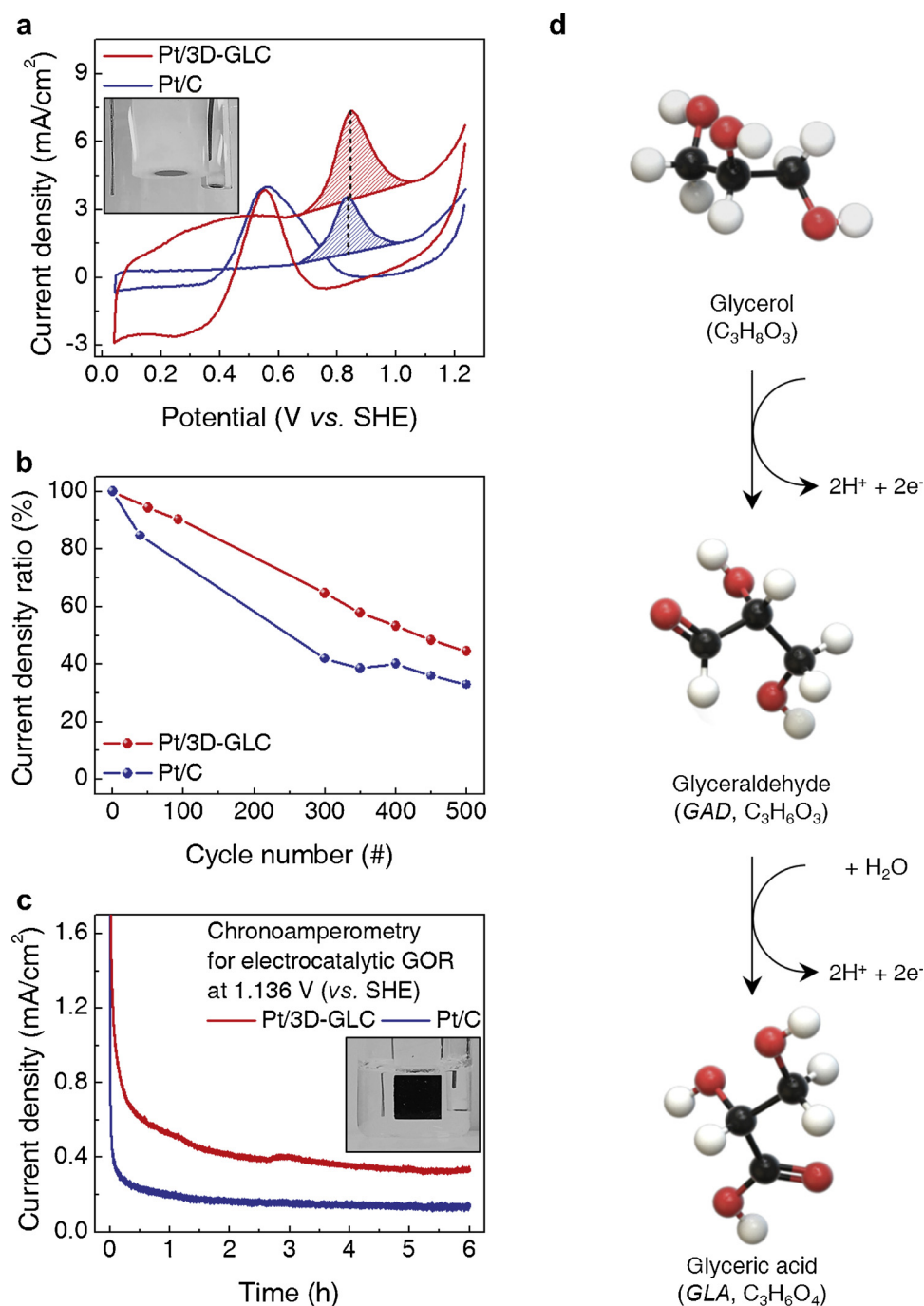
Fig. 5. Electrochemical performance analysis of Pt/3D-GLC and Pt/C for the electrocatalytic GOR in both electrochemical half-cell and batch reactor systems. a, CV curves for the electrocatalytic GOR over Pt/3D-GLC and Pt/C in N_2-purged 2 M glycerol + 0.5 M H_2SO_4 solution at room temperature. The inset digital photograph displays an electrochemical half-cell system having a three electrode configuration. Note that the forward peaks for the electrocatalytic GOR and their height are depicted with diagonal and short-dashed lines, respectively. b, CV cycle stability toward the electrocatalytic GOR over Pt/3D-GLC and Pt/C. c, Chronoamperometry at anode potential of 1.136 V (*vs.* SHE) in 0.1 M glycerol + 0.5 M H_2SO_4 solution at 60 °C for the electrocatalytic GOR over Pt/3D-GLC and Pt/C loaded on a carbon paper electrode. The inset digital photograph exhibits an electrochemical batch reactor system having a three electrode configuration. d, Observed reaction pathway for the electrocatalytic GOR using an electrochemical batch reactor system at 60 °C after reaction of 6 h.

Table 4
Summary of the electrocatalytic GOR performance using an electrochemical half-cell system at room temperature.

Samples	Feed solution	Tafel slope (mV/dec)	Forward peak		Reverse peak		I_f/I_r ratio
			Peak position (V *vs.* SHE)	I_f (mA/cm^2)	Peak position (V *vs.* SHE)	I_r (mA/cm^2)	
Pt/3D-GLC	N_2-purged 2 M glycerol/0.5 M H_2SO_4	171.28	0.85	3.92	0.56	5.25	0.75
Pt/C		201.83	0.84	2.50	0.56	4.19	0.60

catalyst for catalytic GOR was evaluated in an electrochemical half-cell system featuring the catalyst-deposited glassy carbon electrode (geometric area: *ca.* 0.071 cm^2) as a working electrode (Fig. 5a and b). For comparison, a commercial Pt/C was also examined under the same electrochemical reaction conditions. Electrocatalytic GOR performance was measured and evaluated by using the CV technique in a N_2-purged

2 M glycerol + 0.5 M H_2SO_4 solution at room temperature (Fig. 5a, b, S17, and S18, and Table 4). The CV curves for both Pt/3D-GLC and Pt/C have two respective anodic current peaks during positive and negative sweeps. In detail, one anodic current peak in the positive sweep (forward peak) is attributed to the electrochemical oxidation of glycerol; the other anodic current peak during the negative sweep (reverse peak)

is related to the subsequent electrooxidation of glycerol on the metallic catalyst surfaces after reduction of surface metal oxides. As depicted in Fig. 5a and summarized in Table 4, the net forward peak current density (I_f) of Pt/3D-GLC was 1.6-fold higher than that of Pt/C. To understand how the reaction kinetics changes with different catalysts, we calculated the Tafel slopes for electrocatalytic GOR over Pt/3D-GLC and Pt/C: a lower Tafel slope indicates faster electrocatalytic reaction kinetics [60]. As presented in Table 4, Pt/3D-GLC and Pt/C showed Tafel slope values of 171.28 and 201.83 mV/dec, respectively. This implies that, compared to Pt/C, Pt/3D-GLC leads to enhanced GOR kinetics. In addition, the ratio of net current densities of forward and reverse peaks (I_f/I_r) for Pt/3D-GLC demonstrated a larger I_f/I_r value than that for Pt/C, suggesting that the catalyst surface is relatively less poisoned by accretion of intermediates during GOR over Pt/3D-GLC. These results indicate that the Pt/3D-GLC can serve as a superior electrocatalyst for the GOR in terms of good electrochemical glycerol oxidation performance and the poisoning tolerance toward carbonaceous intermediates [24]. The CV cycle stability for the GOR was tested and examined for the Pt/3D-GLC and Pt/C samples. Fig. 5b confirms that the stability of the Pt/3D-GLC was enhanced compared to Pt/C. The prepared Pt/3D-GLC catalyst also had a lower deactivation rate than the commercial Pt/C catalyst, indicating that the former was more durable than Pt/C for the electrochemical GOR.

For further investigation of the electrochemical GOR performance of Pt/3D-GLC and Pt/C samples, an electrochemical batch reactor system having catalyst-coated carbon paper (geometric area: *ca.* 2 cm^2) as the working electrode was designed and used for the testing (Fig. 5c and d). For the GOR in a batch reactor system, chronoamperometry was carried out at a fixed potential of 1.136 V (*vs.* SHE) for 6 h in a N$_2$-purged 0.1 M glycerol + 0.5 M H$_2$SO$_4$ solution at a reaction temperature of 60 °C (Fig. 5c and d). We chose this potential value because glycerol conversion increased with increase of potential from 0.7 to 1.2 V (*vs.* SHE) due to the use of catalyst coated carbon paper electrodes in our electrochemical batch reactor system, as reported in our previous works [4,9]. The recorded current density *vs.* time plots for the GOR over Pt/3D-GLC and Pt/C catalysts coated on carbon paper electrodes yielded similar results to those obtained from the CV experiments in the half-cell system. The Pt/3D-GLC produced higher current density as compared to commercial Pt/C throughout the chronoamperometry measurements, verifying its remarkable GOR activity (Fig. 5c). Moreover, to compare kinetic activities of prepared catalysts, we calculated turnover frequencies (TOFs) based on H$_2$ chemisorption measurement and chronoamperometry results in the electrochemical batch reactor system (Table S2). The calculated TOFs for Pt/3D-GLC and Pt/C were 31.99 and 11.01 h^{-1}, respectively. The TOF value of Pt/3D-GLC is about 2.91 times higher than that of Pt/C, which proves that the reaction kinetics of Pt/3D-GLC is better than that of commercial Pt/C. After the electrochemical reaction in the batch reactor, the resultant liquid reaction products were analyzed *via* HPLC in order to determine how many glycerol molecules are converted and which products are generated from the GOR over Pt/3D-GLC and Pt/C catalysts. As depicted in HPLC chromatograms (Fig. S19) and summarized in Table S2, the Pt/3D-GLC converted a greater amount of glycerol than Pt/C: the values of glycerol conversion for Pt/3D-GLC and Pt/C were 7.7 and 2.3%, respectively. In addition, the Pt/3D-GLC catalyst produced a more oxidized product of glyceric acid (*GLA*) in company with glyceraldehyde (*GAD*) compared to the Pt/C catalyst (Fig. 5d and Table S2). These product analysis results from the electrochemical GOR performed in the batch reactor system also support that the Pt/3D-GLC catalyst possesses superior ability for the electrocatalytic GOR than the commercial Pt/C catalyst.

The enhanced catalytic GOR activity on Pt/3D-GLC can be associated with an increased amount of Pt active sites by the formation of highly dispersed Pt nanoclusters (d_{LN} = 1.25 ± 0.30 nm) on 3D-GLC as shown in the HAADF-STEM images. The electronic structure of the Pt nanoclusters formed on 3D-GLC also changed due to interaction between 3D-GLC support and impregnated Pt nanoclusters; Raman, XPS,

and XANES spectra revealed changes in the Pt electronic features due to Pt nanocluster and 3D-GLC support interaction. Therefore, the glycerol molecules on the structurally and electronically-modified Pt nanocluster surface with 3D-GLC may be efficiently oxidized by controlling the adsorption/desorption properties of glycerol and the other generated products [8,20], eventually affecting the catalytic GOR activity. As shown in this study, excellent catalytic performance for GOR was obtained on the Pt/3D-GLC catalyst compared to commercial Pt/C, and the Pt/3D-GLC catalyst was modified structurally and electronically by interaction between the Pt nanoclusters and the graphene-like surface. Based on the experimental results with catalyst performance testing and various physicochemical characterizations, theoretical insights obtained for our designed Pt/3D-GLC are discussed starting in the next section regarding how this Pt/3D-GLC can be efficient for the GOR compared to the conventional Pt/C.

3.6. Theoretical investigation of why the Pt/3D-GLC shows improved electrocatalytic GOR performance

DFT calculations were performed to demonstrate that the enhanced GOR performance of Pt/3D-GLC may be due to decreasing Pt cluster size and structural changes by forming an interface between the Pt cluster and the graphene-like surface *via* our novel synthesis technique, as described above. This calculation is included to expand upon the currently hypothesized Pt size and 3D-GLC support effects based on the catalysts' properties observed in this study using STEM, Raman, XPS, XANES, and EXAFS analyses. In order to model the Pt size and support effects, DFT designs of the carbon-supported Pt catalysts (*i.e.* Pt$_{13}$/ graphite, Pt$_{13}$/graphene, Pt$_{55}$/graphite, and Pt$_{55}$/graphene) and glycerol were carried out and presented in slab models (Fig. 6). Note that the Pt$_{13}$ and Pt$_{55}$ clusters comprise 13 and 55 Pt atoms arranged in a cuboctahedral particle structure, respectively. Relaxation of the Pt clusters was conducted in the DFT method to produce a thermodynamically favorable structure having minimized internal energy, and then the Pt clusters were put on the graphite and graphene supports to reduce the computational cost and to investigate structural changes of Pt and carbon supports. After the geometric relaxation of the initial slab models for the carbon-supported Pt catalysts, we measured the alternation of adjacent carbon–carbon (C–C) and Pt–Pt interatomic distances, which were at the interfaces between the carbon supports and the Pt clusters (Figs. S20 and S21, and Table 5). In detail, before relaxation, pristine graphite and graphene had the same evaluated value for a C–C distance of 1.42 Å. At the Pt(111) crystal surfaces, the Pt–Pt distances for pure Pt$_{13}$ and Pt$_{55}$ clusters (*i.e.* without carbon supports) were 2.67 and 2.83 Å, respectively. After the geometric relaxation of the carbon-supported Pt models, the C–C and Pt–Pt distances in the case of Pt$_{13}$/graphene were significantly expanded to 1.45–1.46 Å and to 2.90–3.65 Å, respectively. Compared to Pt$_{13}$/graphene, Pt$_{13}$/graphite was relatively less expanded in terms of the C–C and Pt–Pt distances, which were 1.44–1.45 Å and 2.91–3.60 Å, respectively. For the case of Pt$_{55}$ clusters, the C–C distances were expanded and compressed for Pt$_{55}$/graphene and Pt$_{55}$/graphite, respectively. On both supports, the interatomic distances between adjacent Pt atoms that are touched with the carbon supports were compressed.

The most stable binding configuration of glycerol molecules on Pt clusters was determined by estimating the binding energy values (ΔE_{BE}) of a glycerol molecule onto a Pt surface for different configurations of the glycerol molecule onto Pt(100) and Pt(111) crystal surfaces (Fig. S22). On the Pt(111) crystal surface, two horizontal configurations are not favorable for glycerol to bind on the Pt crystal surface due to the positive ΔE_{BE} values (*i.e.* endothermic), whereas the vertically bound glycerol is somewhat favorable to bind on Pt because of the small ΔE_{BE} value of −0.012 eV. Similar with the Pt(111) surface, glycerol strongly binds on the Pt(100) crystal surface with the vertical configuration, exhibiting the lowest ΔE_{BE} value of −0.127 eV. Based on the results in Fig. S22, we concluded that the most stable binding configuration of
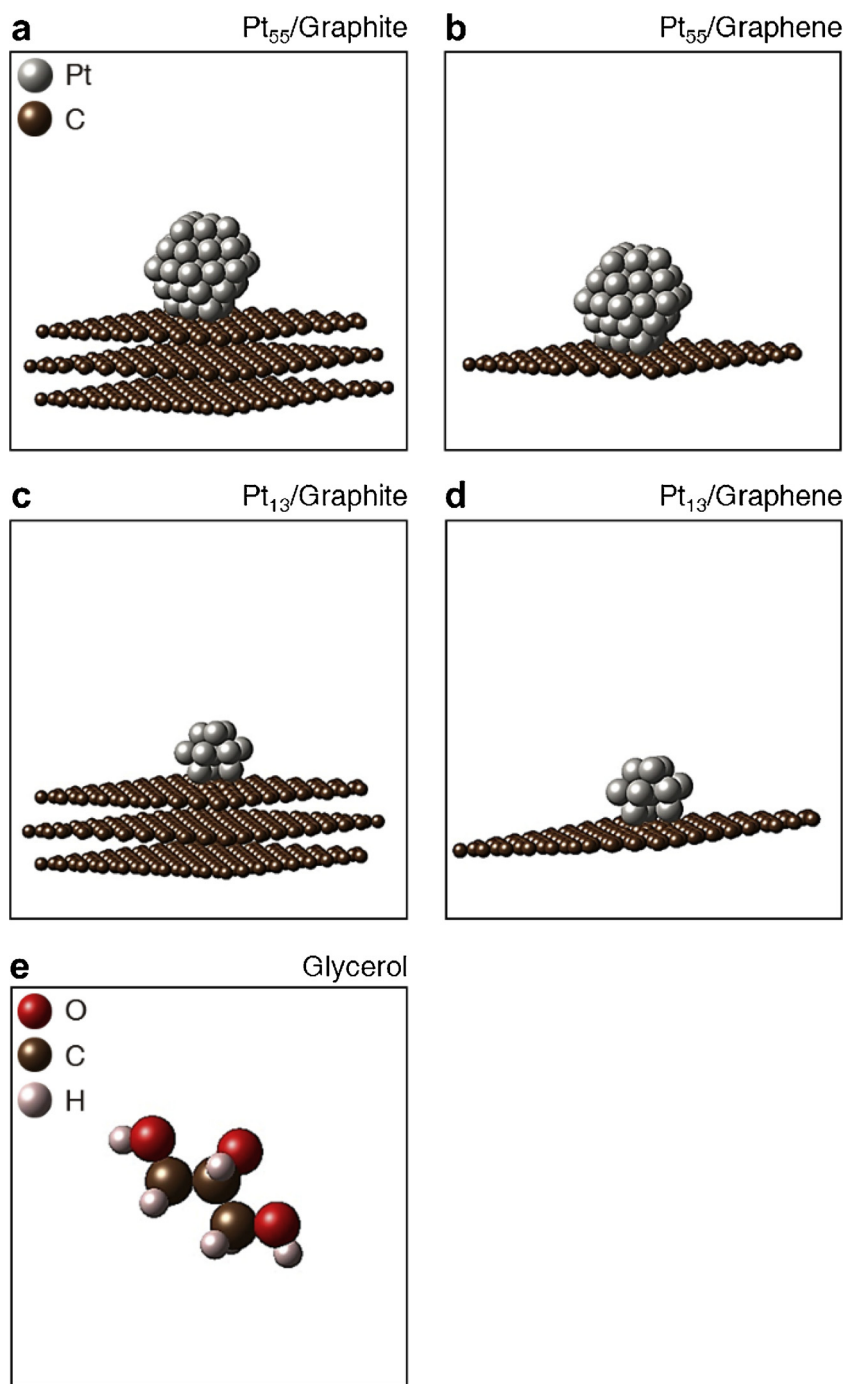
Fig. 6. DFT model structures of Pt/3D-GLC, Pt/C, and glycerol molecule for theoretical elaboration of the electrocatalytic GOR performance difference *via ab-initio* simulations. a–e, Corresponding slab models for Pt_{55}/Graphite (a), Pt_{55}/Graphene (b), Pt_{13}/Graphite (c), Pt_{13}/Graphene (d), and glycerol (e).

Table 5
Summary of the selected interatomic distances between adjacent atoms in slab models for carbon-supported Pt catalysts in Figs. 6 and S20.

Samples	C−C_A[b] (Å)	C−C_B[b] (Å)	C−C_C[b] (Å)	Pt−Pt[c] (Å)	Difference in C−C distances after relaxation
Pt_{55}/Carbon[a]	1.42	1.42	1.42	2.83	Pristine[a]
Pt_{13}/Carbon[a]	1.42	1.42	1.42	2.67	Pristine[a]
Pt_{55}/Graphite	1.41	1.42	1.42	2.77	Compressed
Pt_{55}/Graphene	1.42	1.43	1.43	2.76	Expanded
Pt_{13}/Graphite	1.44	1.45	1.45	3.60	Expanded
Pt_{13}/Graphene	1.45	1.46	1.45	3.65	Further expanded

[a] The initial slab models for carbon-supported Pt catalysts before relaxation.
[b] The interatomic distances between juxtaposed carbon atoms being in contact with the platinum clusters as presented in Fig. S20.
[c] The interatomic distances between adjacent platinum atoms that are touch with the carbon supports.
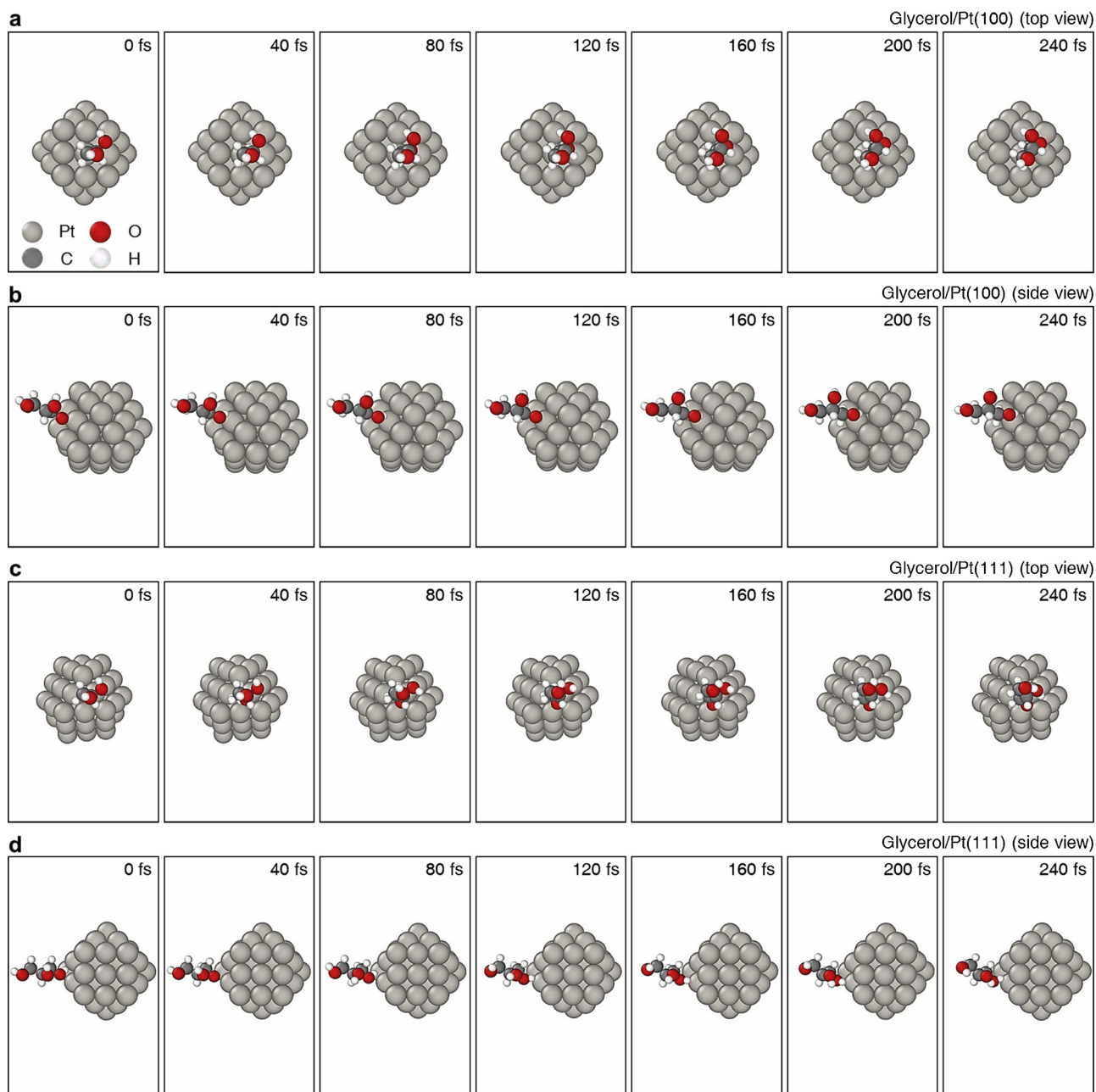
Fig. 7. *Ab-initio* MD simulations for the identification of the thermodynamically stable binding sites of glycerol on Pt(100) and Pt(111) crystal surfaces. a–d Time-series images of slab models exhibiting the evolution of the thermodynamically stable configurations of glycerol on Pt(100) (a,b) and Pt(111) (c,d) crystal surfaces from top (a,c) and side (b,d) views.

glycerol molecules onto Pt crystal surfaces is the vertical orientation of glycerol with respect to the Pt crystal surface. In addition, *ab-initio* MD simulations confirm that glycerol molecule can migrate into the hollow sites on the Pt(100) and Pt(111) crystal surfaces, and these hollow sites can be regarded as the thermodynamically most favorable sites for glycerol binding on the Pt surface (Fig. 7).

As described above, the thermodynamically most stable configuration of the glycerol molecule on the Pt crystal surface was the vertically binding glycerol molecule on the hollow site of the Pt(100) crystal surface. Based on this stable configuration, Fig. 8 presents a summary and a comparison of the adsorption energy of glycerol onto carbon-supported Pt surface values (ΔE_{ads}) in different configurations, where glycerol binds onto the hollow sites at the upper or bottom parts of the Pt(100) surface from Pt clusters on carbon supports. As depicted in Fig. 8, the estimated ΔE_{ads} values for bottom binding of Pt$_{55}$ clusters

were evaluated at -0.578 eV for the graphite support and -1.273 eV for the graphene support. The ΔE_{ads} values at the same site of Pt$_{13}$ clusters were -1.628 eV and -2.131 eV on graphite and graphene, respectively; this tendency is also found at the upper binding cases. These results suggest that glycerol molecules strongly bind on the smaller Pt clusters compared to larger Pt clusters. The smaller particles have a relatively high surface energy; thus, glycerol has to be strongly adsorbed on the Pt surface to minimize the surface energy. Further-more, by comparison of ΔE_{ads} values for Pt clusters on graphite and graphene supports, the glycerol is the most favorable to bind on gra-phene-supported Pt clusters in comparison with Pt clusters on graphite. This can be explained by the geometric and electronic structure changes of the Pt clusters on the different supports. The C–C and Pt–Pt bond distances were comparatively extended compared to those on graphite when Pt cluster was deposited on the graphene surface, as shown in
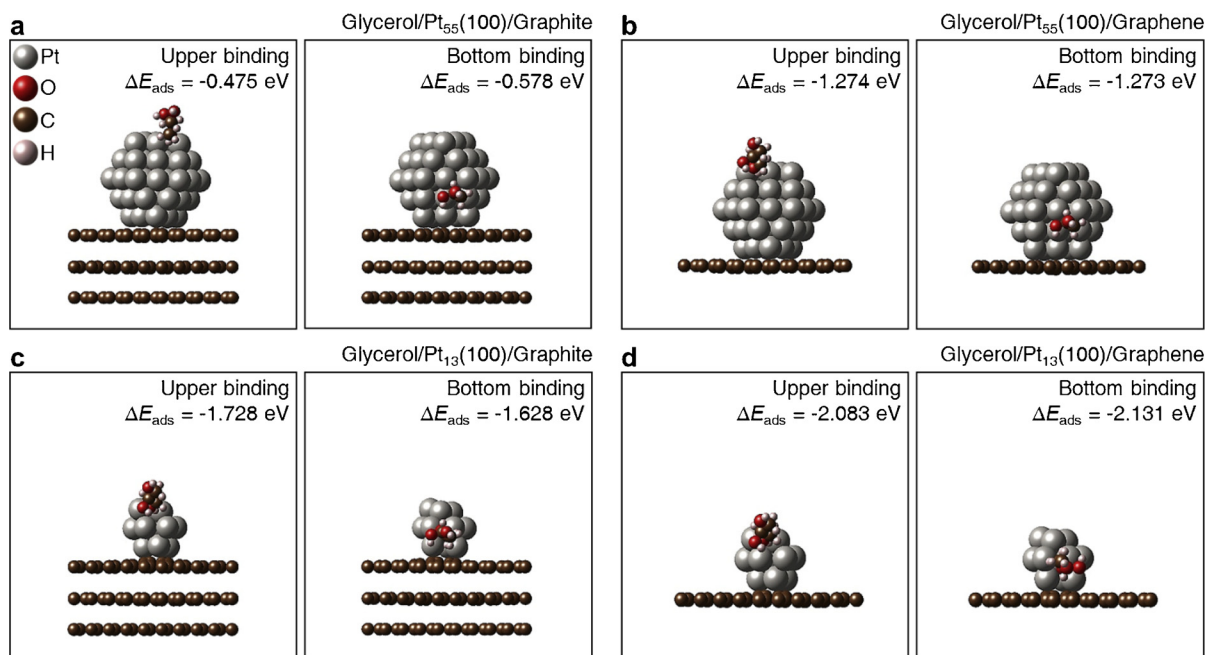
Fig. 8. *Ab-initio* simulations for calculating glycerol adsorption energy related to performance change in electrocatalytic GOR on model structures of Pt/3D-GLC and Pt/C. a–d, Slab models manifesting the thermodynamically stable configurations of glycerol bounded to the upper (left) and bottom (right) sites of the Pt(100) crystal surface from the platinum clusters in Pt_{55}/Graphite (a), Pt_{55}/Graphene (b), Pt_{13}/Graphite (c), and Pt_{13}/Graphene (d). Note that estimated ΔE_{ads} values are presented for corresponding configurations.

Figs. S20, S21, and Table 5. This beneficial geometric change can lead to a change of electronic structure and result in enhanced adsorption of glycerol. We recently reported that there exists a volcano-type relation between the theoretically calculated values of the glycerol binding energy and the experimentally obtained values of the onset potential for GOR over Pt and PtRu catalyst systems [8]. In our previous work we concluded that enhanced adsorption of glycerol on a Pt surface modified with Ru brings about improved glycerol oxidation kinetics because glycerol has an excessively weak ΔE_{ads} onto a surface of Pt only. Accordingly, the desired strategy for designing GOR catalysts is to increase the ΔE_{ads} for glycerol on the catalyst surface [8,20,61]. In this work, in contrast to Vulcan XC-72-supported larger Pt nanoparticles, our finely dispersed Pt nanoclusters (1.25 ± 0.30 nm) supported on 3D graphene-like carbon can give rise to excellent GOR activity in accordance with the strong glycerol adsorption behavior on its Pt crystal surfaces.

4. Conclusions

In summary, we successfully synthesized highly-dispersed Pt nanoclusters supported on 3D-GLC by using zeolite template based carbon synthesis and subsequent Pt impregnation methods. The prepared Pt/3D-GLC catalytic material was used and tested for electrochemical GOR. The large surface area and abundant oxygen functional groups on the surface of 3D-GLC support enabled the creation of fine Pt nanoclusters (*ca.* 1.25 ± 0.30 nm) uniformly dispersed on 3D-GLC. Compared to commercial Pt/C, changes in structural and electronic features of Pt/3D-GLC were observed by STEM, Raman, XPS, XANES, and EXAFS analyses, and they were associated with the interaction between the Pt nanocluster and 3D-GLC support. The structurally and electronically-modified Pt/3D-GLC catalyst demonstrated excellent GOR activity and stability in comparison with commercial Pt/C, and also generated a more oxidized product of *GLA* during the oxidation process at the same reaction conditions. This enhanced GOR performance of Pt/3D-GLC was due to the increase of Pt active sites by decreasing the Pt cluster size and the change in the structural and electronic properties of the Pt by interaction between the Pt cluster and 3D-GLC. In this work, the ΔE_{ads} values of glycerol onto carbon-supported Pt

clusters, the representative indicator of the GOR activity, were theoretically calculated and estimated by first-principle DFT and *ab-initio* MD simulations. It was observed that glycerol molecules were strongly bound on the Pt surfaces by (i) decreasing the Pt cluster size and (ii) using a graphene support instead of a graphite support. The high-surface-energy small Pt particles result in strong adsorption of glycerol on the Pt surface, minimizing the Pt surface energy. In addition, the extended C−C and Pt−Pt bond distances in the graphene-supported Pt nanoclusters can bring about changes in the electronic structure, promoting the adsorption of glycerol. The computational simulation results suggest that our newly designed Pt/3D-GLC can lead to superior GOR catalytic performance, in agreement with the enhanced glycerol adsorption behavior on the Pt crystal surfaces. This work shows how metal nanoclusters designed with a better catalyst support material can be used to enhance catalytic performance in electrochemical oxidation reactions. In addition, this facile and effective method of synthesizing finely-dispersed metal nanoclusters on a unique carbon support can be widely adopted for designing and developing efficient materials for various kinds of electrochemical applications.

Appendix A. Supplementary data

Supplementary material related to this article can be found, in the online version, at doi:https://doi.org/10.1016/j.apcatb.2019.01.022.

References

[1] S.K. Green, G.A. Tompsett, H.J. Kim, W.B. Kim, G.W. Huber, Electrocatalytic reduction of acetone in a proton-exchange-membrane reactor: a model reaction for the electrocatalytic reduction of biomass, ChemSusChem 5 (2012) 2410–2420, https://doi.org/10.1002/cssc.201200416.

[2] Z. Zhang, L. Xin, W. Li, Electrocatalytic oxidation of glycerol on Pt/C in anion-exchange membrane fuel cell: cogeneration of electricity and valuable chemicals, Appl. Catal. B 119–120 (2012) 40–48, https://doi.org/10.1016/j.apcatb.2012.02.009.

[3] Z. Li, S. Kelkar, C.H. Lam, K. Luczek, J.E. Jackson, D.J. Miller, C.M. Saffron, Aqueous electrocatalytic hydrogenation of furfural using a sacrificial anode, Electrochim. Acta 64 (2012) 87–93, https://doi.org/10.1016/j.electacta.2011.12.105.

[4] H.J. Kim, J. Lee, S.K. Green, G.W. Huber, W.B. Kim, Selective glycerol oxidation by electrocatalytic dehydrogenation, ChemSusChem 7 (2014) 1051–1056, https://doi.org/10.1002/cssc.201301218.

[5] J. Qi, L. Xin, D.J. Chadderdon, Y. Qiu, Y. Jiang, N. Benipal, C. Liang, W. Li, Electrocatalytic selective oxidation of glycerol to tartronate on Au/C anode catalysts in anion exchange membrane fuel cells with electricity cogeneration, Appl. Catal. B 154–155 (2014) 360–368, https://doi.org/10.1016/j.apcatb.2014.02.040.

[6] H.G. Cha, K.-S. Choi, Combined biomass valorization and hydrogen production in a photoelectrochemical cell, Nat. Chem. 7 (2015) 328–333, https://doi.org/10.1038/nchem.2194.

[7] S. Lee, H.J. Kim, E.J. Lim, Y. Kim, Y. Noh, G.W. Huber, W.B. Kim, Highly selective transformation of glycerol to dihydroxyacetone without using oxidants by a PtSb/C-catalyzed electrooxidation process, Green Chem. 18 (2016) 2877–2887, https://doi.org/10.1039/C5GC02865E.

[8] Y. Kim, H.W. Kim, S. Lee, J. Han, D. Lee, J.-R. Kim, T.-W. Kim, C.-U. Kim, S.-Y. Jeong, H.-J. Chae, B.-S. Kim, H. Chang, W.B. Kim, S.M. Choi, H.J. Kim, The role of ruthenium on carbon-supported PtRu catalysts for electrocatalytic glycerol oxidation under acidic conditions, ChemCatChem 9 (2017) 1683–1690, https://doi.org/10.1002/cctc.201601325.

[9] H.J. Kim, Y. Kim, D. Lee, J.-R. Kim, H.-J. Chae, S.-Y. Jeong, B.-S. Kim, J. Lee, G.W. Huber, J. Byun, S. Kim, J. Han, Coproducing value-added chemicals and hydrogen with electrocatalytic glycerol oxidation technology: experimental and techno-economic investigations, ACS Sustain. Chem. Eng. 5 (2017) 6626–6634, https://doi.org/10.1021/acssuschemeng.7b00868.

[10] M.J. Kang, H. Park, J. Jegal, S.Y. Hwang, Y.S. Kang, H.G. Cha, Electrocatalysis of 5-hydroxymethylfurfural at cobalt based spinel catalysts with filamentous nanoarchitecture in alkaline media, Appl. Catal. B 242 (2019) 85–91, https://doi.org/10.1016/j.apcatb.2018.09.087.

[11] T. Rafaïdeen, S. Baranton, C. Coutanceau, Highly efficient and selective electro-oxidation of glucose and xylose in alkaline medium at carbon supported Alloyed PdAu nanocatalysts, Appl. Catal. B (2018), https://doi.org/10.1016/j.apcatb.2018.11.006.

[12] G.W. Huber, S. Iborra, A. Corma, Synthesis of transportation fuels from biomass: chemistry, catalysts, and engineering, Chem. Rev. 106 (2006) 4044–4098, https://doi.org/10.1021/cr068360d.

[13] J. Callison, N.D. Subramanian, S.M. Rogers, A. Chutia, D. Gianolio, C.R.A. Catlow, P.P. Wells, N. Dimitratos, Directed aqueous-phase reforming of glycerol through tailored platinum nanoparticles, Appl. Catal. B 238 (2018) 618–628, https://doi.org/10.1016/j.apcatb.2018.07.008.

[14] S. He, I. Muizebelt, A. Heeres, N.J. Schenk, R. Blees, H.J. Heeres, Catalytic pyrolysis of crude glycerol over shaped ZSM-5/bentonite catalysts for bio-BTX synthesis, Appl. Catal. B 235 (2018) 45–55, https://doi.org/10.1016/j.apcatb.2018.04.047.

[15] Q. Xie, S. Li, R. Gong, G. Zheng, Y. Wang, P. Xu, Y. Duan, S. Yu, M. Lu, W. Ji, Y. Nie, J. Ji, Microwave-assisted catalytic dehydration of glycerol for sustainable production of acrolein over a microwave absorbing catalyst, Appl. Catal. B 243 (2019) 455–462, https://doi.org/10.1016/j.apcatb.2018.10.058.

[16] W. Zhou, J. Luo, Y. Wang, J. Liu, Y. Zhao, S. Wang, X. Ma, WOx domain size, acid properties and mechanistic aspects of glycerol hydrogenolysis over Pt/WOx/ZrO2, Appl. Catal. B 242 (2019) 410–421, https://doi.org/10.1016/j.apcatb.2018.10.006.

[17] R. Ciriminna, C.D. Pina, M. Rossi, M. Pagliaro, Understanding the glycerol market, Eur. J. Lipid Sci. Technol. 116 (2014) 1432–1439, https://doi.org/10.1002/ejlt.201400229.

[18] M.R.K. Estahbanati, M. Feilizadeh, M.C. Iliuta, Photocatalytic valorization of glycerol to hydrogen: optimization of operating parameters by artificial neural network, Appl. Catal. B 209 (2017) 483–492, https://doi.org/10.1016/j.apcatb.2017.03.016.

[19] M. Simões, S. Baranton, C. Coutanceau, Electrochemical valorisation of glycerol, ChemSusChem 5 (2012) 2106–2124, https://doi.org/10.1002/cssc.201200335.

[20] J. Han, Y. Kim, H.W. Kim, D.H.K. Jackson, D. Lee, H. Chang, H.-J. Chae, K.-Y. Lee, H.J. Kim, Effect of atomic-layer-deposited TiO2 on carbon-supported Ni catalysts for electrocatalytic glycerol oxidation in alkaline media, Electrochem. Commun. 83 (2017) 46–50, https://doi.org/10.1016/j.elecom.2017.08.023.

[21] K. Yamamoto, T. Imaoka, W.-J. Chun, O. Enoki, H. Katoh, M. Takenaga, A. Sonoi, Size-specific catalytic activity of platinum clusters enhances oxygen reduction reactions, Nat. Chem. 1 (2009) 397–402, https://doi.org/10.1038/nchem.288.

[22] G.L. Caneppele, T.S. Almeida, C.R. Zanata, É. Teixeira-Neto, P.S. Fernández, G.A. Camara, C.A. Martins, Exponential improving in the activity of Pt/C nanoparticles towards glycerol electrooxidation by Sb ad-atoms deposition, Appl. Catal. B 200 (2017) 114–120, https://doi.org/10.1016/j.apcatb.2016.06.072.

[23] J.H. Kim, S.M. Choi, S.H. Nam, M.H. Seo, S.H. Choi, W.B. Kim, Influence of Sn content on PtSn/C catalysts for electrooxidation of C1–C3 alcohols: synthesis,

[24] H.J. Kim, S.M. Choi, S. Green, G.A. Tompsett, S.H. Lee, G.W. Huber, W.B. Kim, Highly active and stable PtRuSn/C catalyst for electrooxidations of ethylene glycol and glycerol, Appl. Catal. B 101 (2011) 366–375, https://doi.org/10.1016/j.apcatb.2010.10.005.

[25] M. Roca-Ayats, O. Guillén-Villafuerte, G. García, M. Soler-Vicedo, E. Pastor, M.V. Martínez-Huerta, PtSn nanoparticles supported on titanium carbonitride for the ethanol oxidation reaction, Appl. Catal. B 237 (2018) 382–391, https://doi.org/10.1016/j.apcatb.2018.05.078.

[26] S.H. Joo, S.J. Choi, I. Oh, J. Kwak, Z. Liu, O. Terasaki, R. Ryoo, Ordered nanoporous arrays of carbon supporting high dispersions of platinum nanoparticles, Nature 412 (2001) 169–172, https://doi.org/10.1038/35084046.

[27] S.M. Choi, M.H. Seo, H.J. Kim, W.B. Kim, Synthesis of surface-functionalized graphene nanosheets with high Pt-loadings and their applications to methanol electrooxidation, Carbon 49 (2011) 904–909, https://doi.org/10.1016/j.carbon.2010.10.055.

[28] M.H. Seo, S.M. Choi, H.J. Kim, W.B. Kim, The graphene-supported Pd and Pt catalysts for highly active oxygen reduction reaction in an alkaline condition, Electrochem. Commun. 13 (2011) 182–185, https://doi.org/10.1016/j.elecom.2010.12.008.

[29] H.J. Kim, S.M. Choi, M.H. Seo, S. Green, G.W. Huber, W.B. Kim, Efficient electrooxidation of biomass-derived glycerol over a graphene-supported PtRu electrocatalyst, Electrochem. Commun. 13 (2011) 890–893, https://doi.org/10.1016/j.elecom.2011.05.031.

[30] C. Zhai, M. Sun, L. Zeng, M. Xue, J. Pan, Y. Du, M. Zhu, Construction of Pt/graphitic C3N4/MoS2 heterostructures on photo-enhanced electrocatalytic oxidation of small organic molecules, Appl. Catal. B 243 (2019) 283–293, https://doi.org/10.1016/j.apcatb.2018.10.047.

[31] R.C.P. Oliveira, J. Milikić, E. Daş, A.B. Yurtcan, D.M.F. Santos, B. Šljukić, Platinum/polypyrrole-carbon electrocatalysts for direct borohydride-peroxide fuel cells, Appl. Catal. B 238 (2018) 454–464, https://doi.org/10.1016/j.apcatb.2018.06.057.

[32] F.J. García-Mateos, T. Cordero-Lanzac, R. Berenguer, E. Morallón, D. Cazorla-Amorós, J. Rodríguez-Mirasol, T. Cordero, Lignin-derived Pt supported carbon (submicron)fiber electrocatalysts for alcohol electro-oxidation, Appl. Catal. B 211 (2017) 18–30, https://doi.org/10.1016/j.apcatb.2017.04.008.

[33] A. Zubiaur, N. Job, Streamlining of the synthesis process of Pt/carbon xerogel electrocatalysts with high Pt loading for the oxygen reduction reaction in proton exchange membrane fuel cells applications, Appl. Catal. B 225 (2018) 364–378, https://doi.org/10.1016/j.apcatb.2017.11.059.

[34] M.H. Seo, S.M. Choi, J.K. Seo, S.H. Noh, W.B. Kim, B. Han, The graphene-supported palladium and palladium–yttrium nanoparticles for the oxygen reduction and ethanol oxidation reactions: experimental measurement and computational validation, Appl. Catal. B 129 (2013) 163–171, https://doi.org/10.1016/j.apcatb.2012.09.005.

[35] S.M. Choi, M.H. Seo, H.J. Kim, W.B. Kim, Synthesis and characterization of graphene-supported metal nanoparticles by impregnation method with heat treatment in H2 atmosphere, Synth. Met. 161 (2011) 2405–2411, https://doi.org/10.1016/j.synthmet.2011.09.008.

[36] M.H. Seo, S.M. Choi, E.J. Lim, I.H. Kwon, J.K. Seo, S.H. Noh, W.B. Kim, B. Han, Toward new fuel cell support materials: a theoretical and experimental study of nitrogen-doped graphene, ChemSusChem 7 (2014) 2609–2620, https://doi.org/10.1002/cssc.201402258.

[37] D. Li, M.B. Müller, S. Gilje, R.B. Kaner, G.G. Wallace, Processable aqueous dispersions of graphene nanosheets, Nat. Nanotechnol. 3 (2008) 101–105, https://doi.org/10.1038/nnano.2007.451.

[38] Y.-S. Wang, S.-Y. Yang, S.-M. Li, H.-W. Tien, S.-T. Hsiao, W.-H. Liao, C.-H. Liu, K.-H. Chang, C.-C.M. Ma, C.-C. Hu, Three-dimensionally porous graphene–carbon nanotube composite-supported PtRu catalysts with an ultrahigh electrocatalytic activity for methanol oxidation, Electrochim. Acta 87 (2013) 261–269, https://doi.org/10.1016/j.electacta.2012.09.013.

[39] K. Kim, T. Lee, Y. Kwon, Y. Seo, J. Song, J.K. Park, H. Lee, J.Y. Park, H. Ihee, S.J. Cho, R. Ryoo, Lanthanum-catalysed synthesis of microporous 3D graphene-like carbons in a zeolite template, Nature 535 (2016) 131–135, https://doi.org/10.1038/nature18284.

[40] K. Kim, Y. Kwon, T. Lee, S.J. Cho, R. Ryoo, Facile large-scale synthesis of three-dimensional graphene-like ordered microporous carbon via ethylene carbonization in CaX zeolite template, Carbon 118 (2017) 517–523, https://doi.org/10.1016/j.carbon.2017.03.082.

[41] G. Kresse, J. Furthmüller, Efficient iterative schemes for ab initio total-energy calculations using a plane-wave basis set, Phys. Rev. B 54 (1996) 11169–11186, https://doi.org/10.1103/PhysRevB.54.11169.

[42] J.P. Perdew, K. Burke, M. Ernzerhof, Generalized gradient approximation made simple, Phys. Rev. Lett. 77 (1996) 3865–3868, https://doi.org/10.1103/PhysRevLett.77.3865.

[43] P.E. Blöchl, Projector augmented-wave method, Phys. Rev. B 50 (1994) 17953–17979, https://doi.org/10.1103/PhysRevB.50.17953.

[44] A. Le Valant, C. Comminges, F. Can, K. Thomas, M. Houalla, F. Epron, Platinum supported catalysts: predictive CO and H2 chemisorption by a statistical cubocta-hedron cluster model, J. Phys. Chem. C 120 (2016) 26374–26385, https://doi.org/10.1021/acs.jpcc.6b09241.

[45] G. Kresse, J. Hafner, Ab initio molecular dynamics for liquid metals, Phys. Rev. B 47 (1993) 558–561, https://doi.org/10.1103/PhysRevB.47.558.

[46] M. Deschamps, E. Gilbert, P. Azais, E. Raymundo-Piñero, M.R. Ammar, P. Simon, D. Massiot, F. Béguin, Exploring electrolyte organization in supercapacitor electrodes with solid-state NMR, Nat. Mater. 12 (2013) 351–358, https://doi.org/10.

1038/nmat3567.

[47] G. Bergeret, P. Gallezot, Particle size and dispersion measurements, in: G. Ertl, H. Knözinger, F. Schüth, J. Weitkamp (Eds.), Handbook of Heterogeneous Catalysis, Wiley-VCH, Weinheim, Germany, 2008, pp. 738–765.

[48] H. Nishihara, Q.-H. Yang, P.-X. Hou, M. Unno, S. Yamauchi, R. Saito, J.I. Paredes, A. Martínez-Alonso, J.M.D. Tascón, Y. Sato, M. Terauchi, T. Kyotani, A possible buckybowl-like structure of zeolite templated carbon, Carbon 47 (2009) 1220–1230, https://doi.org/10.1016/j.carbon.2008.12.040.

[49] J. Biener, S. Dasgupta, L. Shao, D. Wang, M.A. Worsley, A. Wittstock, J.R.I. Lee, M.M. Biener, C.A. Orme, S.O. Kucheyev, B.C. Wood, T.M. Willey, A.V. Hamza, J. Weissmüller, H. Hahn, T.F. Baumann, Macroscopic 3D nanographene with dynamically tunable bulk properties, Adv. Mater. 24 (2012) 5083–5087, https://doi.org/10.1002/adma.201202289.

[50] H. Zhang, X. Lv, Y. Li, Y. Wang, J. Li, P25-graphene composite as a high performance photocatalyst, ACS Nano 4 (2010) 380–386, https://doi.org/10.1021/nn901221k.

[51] D.R. Dreyer, S. Park, C.W. Bielawski, R.S. Ruoff, The chemistry of graphene oxide, Chem. Soc. Rev. 39 (2010) 228–240, https://doi.org/10.1039/B917103G.

[52] D. Higgins, M.A. Hoque, M.H. Seo, R. Wang, F. Hassan, J.-Y. Choi, M. Pritzker, A. Yu, J. Zhang, Z. Chen, Development and simulation of sulfur-doped graphene supported platinum with exemplary stability and activity towards oxygen reduction, Adv. Funct. Mater. 24 (2014) 4325–4336, https://doi.org/10.1002/adfm.201400161.

[53] K.S. Subrahmanyam, A.K. Manna, S.K. Pati, C.N.R. Rao, A study of graphene decorated with metal nanoparticles, Chem. Phys. Lett. 497 (2010) 70–75, https://doi.org/10.1016/j.cplett.2010.07.091.

[54] S.M. Choi, J.S. Yoon, H.J. Kim, S.H. Nam, M.H. Seo, W.B. Kim, Electrochemical benzene hydrogenation using PtRhM/C (M = W, Pd, or Mo) electrocatalysts over a polymer electrolyte fuel cell system, Appl. Catal. A: Gen. 359 (2009) 136–143, https://doi.org/10.1016/j.apcata.2009.02.048.

[55] G.-f. Long, X.-h. Li, K. Wan, Z.-x. Liang, J.-h. Piao, P. Tsiakaras, Pt/CN-doped electrocatalysts: Superior electrocatalytic activity for methanol oxidation reaction and mechanistic insight into interfacial enhancement, Appl. Catal. B 203 (2017) 541–548, https://doi.org/10.1016/j.apcatb.2016.10.055.

[56] A.C. Garcia, V.A. Paganin, E.A. Ticianelli, CO tolerance of PdPt/C and PdPtRu/C anodes for PEMFC, Electrochim. Acta 53 (2008) 4309–4315, https://doi.org/10.1016/j.electacta.2008.01.006.

[57] H. Yan, Y. Lin, H. Wu, W. Zhang, Z. Sun, H. Cheng, W. Liu, C. Wang, J. Li, X. Huang, T. Yao, J. Yang, S. Wei, J. Lu, Bottom-up precise synthesis of stable platinum dimers on graphene, Nat. Commun. 8 (2017) 1070, https://doi.org/10.1038/s41467-017-01259-z.

[58] X. Cheng, Y. Li, L. Zheng, Y. Yan, Y. Zhang, G. Chen, S. Sun, J. Zhang, Highly active, stable oxidized platinum clusters as electrocatalysts for the hydrogen evolution reaction, Energy Environ. Sci. 10 (2017) 2450–2458, https://doi.org/10.1039/C7EE02537H.

[59] D.C. Koningsberger, D.E. Sayers, An EXAFS study of platinum - oxygen bonds in the metal-support interface of a highly dispersed Pt/Al2O3 catalyst, Solid State Ionics 16 (1985) 23–27, https://doi.org/10.1016/0167-2738(85)90019-0.

[60] Z. Zhang, L. Xin, J. Qi, D.J. Chadderdon, W. Li, Supported Pt, Pd and Au nanoparticle anode catalysts for anion-exchange membrane fuel cells with glycerol and crude glycerol fuels, Appl. Catal. B 136–137 (2013) 29–39, https://doi.org/10.1016/j.apcatb.2013.01.045.

[61] A. Serov, T. Asset, M. Padilla, I. Matanovic, U. Martinez, A. Roy, K. Artyushkova, M. Chatenet, F. Maillard, D. Bayer, C. Cremers, P. Atanassov, Highly-active Pd–Cu electrocatalysts for oxidation of ubiquitous oxygenated fuels, Appl. Catal. B 191 (2016) 76–85, https://doi.org/10.1016/j.apcatb.2016.03.016.